10-1-2024

Characterization of a Carbon Fiber Based Broadband Microwave Absorber

Ha Tran
Portland State University

Branimir Pejcinovic
Portland State University, percyd@pdx.edu

Robert Doneker
TangiTek, LLC

Kent Thompson
TangiTek, LLC

Adithya Ramachandran
TangiTek, LLC

Citation Details

Tran, H., Pejčinović, B., Doneker, R., Thompson, K., & Ramachandran, A. (2024). Characterization of a carbon fiber based broadband microwave absorber. Journal of Materials Science: Materials in Electronics, 35(28).

Characterization of a Carbon-Fiber Based Broadband Microwave Absorber

Ha Tran

tranha@pdx.edu

Portland State University

Branimir Pejcinovic

Portland State University

Robert Doneker

TangiTek, LLC

Kent Thompson

TangiTek, LLC

Adithya Ramachandran

TangiTek, LLC

Research Article

Keywords: Microwave absorber, carbon fiber, ferrite bead, broadband, lightweight, low-cost, X-band, Ku-band, EM simulation, transmission line theory, reflection loss.

Posted Date: June 11th, 2024

DOI: https://doi.org/10.21203/rs.3.rs-4551061/v1

Additional Declarations: The authors declare no competing interests.

Characterization of a Carbon-Fiber Based Broadband Microwave Absorber

Ha Tran[1*], Branimir Pejčinović[1], Robert Doneker[2], Kent Thompson[2], Adithya Ramachandran[2]

[1*]Department of Electrical and Computer Engineering, Portland State University, Portland, OR 97201, U.S.A.
[2]TangiTek, LLC, Portland, OR 97205, U.S.A.

*Corresponding author(s). E-mail(s): tranha@pdx.edu;
Contributing authors: pejcinb@pdx.edu; doneker@tangitek.com; kthompson@tangitek.com; adiram@tangitek.com;

Abstract

This paper reports the development and characterization of a novel ultra-wideband microwave absorber material (MAM) based on vertically aligned carbon fibers and ferrite beads. This specific material combination and manufacturing process allows MAM design that is thin, lightweight, and broadband. The material is prepared using a flocking process in which its components are electrostatically deposited on top of an adhesive substrate. Distinct material properties of the substrate and materials layers require characterization done with two separated layers. The microwave absorption characteristics are studied first by rectangular waveguide measurements at X and Ku bands that yield complex electric permittivity and magnetic permeability of the MAM samples without any metal backing. Here, the sample is measured under transverse electric waves (TE_{10}). Additional analysis is accomplished with full electromagnetic (EM) simulation using a high-frequency structure simulator (HFSS). The scattering parameters (S-parameters) from waveguide measurements and HFSS simulations are compared and excellent agreement is achieved. Extracted material parameters are also used to analytically calculate the reflection loss (RF) based on the transmission line model. The transmission line model shows excellent agreement with the full EM simulation results which should speed up future studies. Finally, the broadband RL performance of MAM was investigated using a free space spot probe system. The results show a MAM with broadband performance of -10 dB RL over the entire X and Ku bands. Overall, this study demonstrates that

MAM developed using magnetically loaded flocked carbon fiber (MLF-CF) has a promising combination of low-cost, lightweight, and broadband performance.

Keywords: Microwave absorber, carbon fiber, ferrite bead, broadband, lightweight, low-cost, X-band, Ku-band, EM simulation, transmission line theory, reflection loss.

1 Introduction

The rapid progress of wireless technologies has brought many benefits, but it has also led to unwanted electromagnetic interference (EMI) and electromagnetic pollution. To minimize the effects of EMI and meet related regulations of the Federal Communications Commission (FCC), researchers are exploring various solutions. Among the most promising options is the use of microwave absorbers. Additionally, microwave absorbers hold significant importance in military applications to provide stealth capabilities allowing objects to be concealed from radar detection. However, to design effective microwave absorbers, it is crucial to understand the material properties of the absorber. Current research has been focusing on developing new materials with superior absorption properties and improving the design of microwave absorbers.

To optimize absorber performance, various methods have been explored, such as utilizing honeycomb structures with different composites and optimizing using effective medium approximations, resulting in a single layer or a multilayer with the absorption bandwidth from a couple of GHz [1] to the entire X-band [2],[3]. Another approach utilized thin layers of SiO_2 over $MnFe_2O_4$ nano-hollow spheres to achieve a 3.1 GHz bandwidth over the 1 to 17 GHz frequency ranges [4]. Multiple layer setups have also been explored, such as a multi-layer design that combines magnetic iron metal (Fe) and silicon carbide (SiC) for 3.8 GHz bandwidth over the X-band [5]. Another optimization approach considers an oblique incidence plane wave to determine optimal thickness for a given frequency and material properties [6]. Additionally, CoSn doping on barium strontium hexagonal ferrites was used to achieve a bandwidth of 2.43 GHz over the X-band by considering different compositions and thicknesses [7]. Furthermore, Nd^{3+} substituted Mg-Cd ferrite enhanced magnetic loss tangent due to spin rotation was used, resulting in a material with 2.21 GHz bandwidth over the X-band [8]. The notable study conducted by Chen et al. utilized chopped carbon fibers (CF) and epoxy resin [9]. Even with the limited production scale of the sample and performing measurements in X-band waveguides with a 0.9 by 0.4 inches cross-section waveguide, they effectively showcased that the vertical carbon fiber and epoxy resin composite achieved a notable -10 dB bandwidth over 2.8 GHz in the X-band. These various approaches for optimizing microwave absorbers again emphasize the increasing importance and need to minimize electromagnetic pollution and meet regulatory requirements.

Typically, the absorption bandwidth is defined at the -10 dB points in the frequency response of an absorber, which is also known as the -10 dB bandwidth (BW). The research discussed above exhibit a limited bandwidth coverage which is just a few GHz in each band of study, as shown in Table 1. In this paper, we present a

novel approach that involves combining dielectric and magnetic materials to develop a microwave absorber that can provide a broader absorption bandwidth. Table 1 summarizes the absorption bandwidth together with the frequency where the best RL performance is obtained. Materials included are mentioned above and are compared with the MLF-CF absorbers: without filler [10, 11] and with filler (this work). We can see that the -10 dB bandwidth of the most recent MLF-CF absorber is broader than others, covering both the X- and Ku- bands from 8 to 18 GHz. In addition to the enhancement in absorption bandwidth, the MLF-CF absorber introduced in this work is much more robust compared to the previous studies due to the addition of filler/encapsulation material. Furthermore, the proposed absorber is easy to manufacture and utilizes commercially available materials such as carbon fiber and ferrite magnetic particles.

Table 1 Comparison of absorption bandwidth (-10dB BW) and the frequency where the best RL performance is obtained (F_{best}) of previously explored absorbers and MLF-CF absorbers.

Absorber structures	-10dB BW (GHz)	F_{best} (GHz)	Reference
Single-layer honeycomb with magnetic micro-powders and epoxy/hardener	2.2	4.4	[1]
Honeycomb sandwich structures	1.5	3.7	[1]
	4.0	9.5	[3]
Triple-layer honeycomb with Fe/SiC composite	3.2	10.3	[2]
Bi-layered nano-hollow spheres using SiO_2 and $MnFe_2O_4$	3.1	11.7	[4]
Multi-layer gradient perforated structure constituted of magnetic iron metal and SiC	3.8	10.2	[5]
Single-layer dielectric-magnetic composites	2.5 - 3	6	[6]
CoSn doped - Barium strontium hexagonal ferrites	2.43	10.88	[7]
Nd^{3+} substituted Mg-Cd spinel ferrites	2.21	10.3	[8]
Vertical carbon fiber and epoxy resin composite	2.8	9	[9]
MLF-CF without filler	2.5	11.1	[10, 11]
MLF-CF with filler	10	10.2	This work

In microwave absorber studies, the extraction of material parameters, i.e., determining the complex values of relative electric permittivity and magnetic permeability, holds significant importance. This process not only provides a deeper insight into the loss mechanisms but also enables the optimization of microwave absorbers for specific frequency bandwidths. To characterize the absorption characteristics of the MLF-CF absorber, this paper employs a commonly used parameter extraction method using rectangular waveguides. Practical considerations of measurement using rectangular waveguides are also discussed.

In the field of material property extraction, the original technique was established by Nicolson and Ross in 1970 [12] and further developed by Weir in 1974 [13]. This Nicolson-Ross-Weir (NRW) technique, commonly employed in rectangular waveguides, is both straightforward to implement and highly accurate. It is widely utilized for

extracting relative permittivity and permeability across various material types and frequency bands. However, a limitation of this technique is that it requires calibrations to move reference planes to the sample under test. In 1990, another extraction method with the concept of reference plane invariance (RPI) was introduced in [14]. While this algorithm was an improvement, it still relied on an iterative process that necessitated an accurate initial guess. Inputting incorrect values could lead to inaccurate results. To address this issue, an explicit RPI method, which does not require interactive steps was proposed in [15]. In this study, we employ the original NRW algorithm to extract material parameters from rectangular waveguide measurements due to its simplicity.

Subsequent sections of this paper are structured as follows: the next section presents an overview of the fundamental components and fabrication process of the proposed magnetically loaded flocked carbon fiber (MLF-CF) absorber. In Section 3, we provide theoretical calculations for the reflection loss. Section 4 demonstrates the rectangular waveguide measurements and extraction of the absorber parameters. The extracted parameters are then used in 3D electromagnetic simulation in Section 5 for comparison with measurement and analytical results. Moving forward, Section 6 describes the free-space reflection loss measurement, its analytical calculation and discussion of the results. Finally, a summary of the findings and future work is presented in Section 7.

2 Material Components and Fabrication Process

The MLF-CF absorber concept involves combining carbon fiber (CF) material with magnetic particles to create unique structures. These structures consist of CF threads anchored to a substrate at one end and magnetic particles attached at the other. We use a process called flocking, where numerous small fiber strands (known as flock) are electrostatically deposited onto an adhesive-coated surface. To achieve this, we utilize commercially available medium modulus polyacrylonitrile (PAN) based chopped CF as flock, which ranges in length from 1 to 3 mm. Additionally, the magnetic material we use is made up of zero-valent carbonyl iron microspheres with diameters between 3 and 10 μm.

Fig. 1 shows a flow chart of the main fabrication steps used to produce magnetically loaded flocked CF absorber (MLF-CF) prototypes together with an illustration of the MF-CF absorber structure at each step:

- **Step 1:** Deposit a 1 mm thick layer of high-loss dielectric material as an adhesive base in the x-y plane.
- **Step 2:** Electrostatically deposit (i.e. flock) carbon fibers (CF) onto the adhesive substrate using a flocking gun. The adhesive substrate is in the horizontal x-y plane, and the CF is deposited with vertical orientation (along the z-axis) relative to the adhesive surface. Fig. 2 demonstrates the flocking process with the profile view of vertically flocked CF.
- **Step 3:** Preserve the vertical CF structure by spray coating it with an insulating layer, ensuring a non-conductive top surface in the x-y plane. This is crucial for achieving high-performance absorbers, and it also insulates the individual CF from each other.

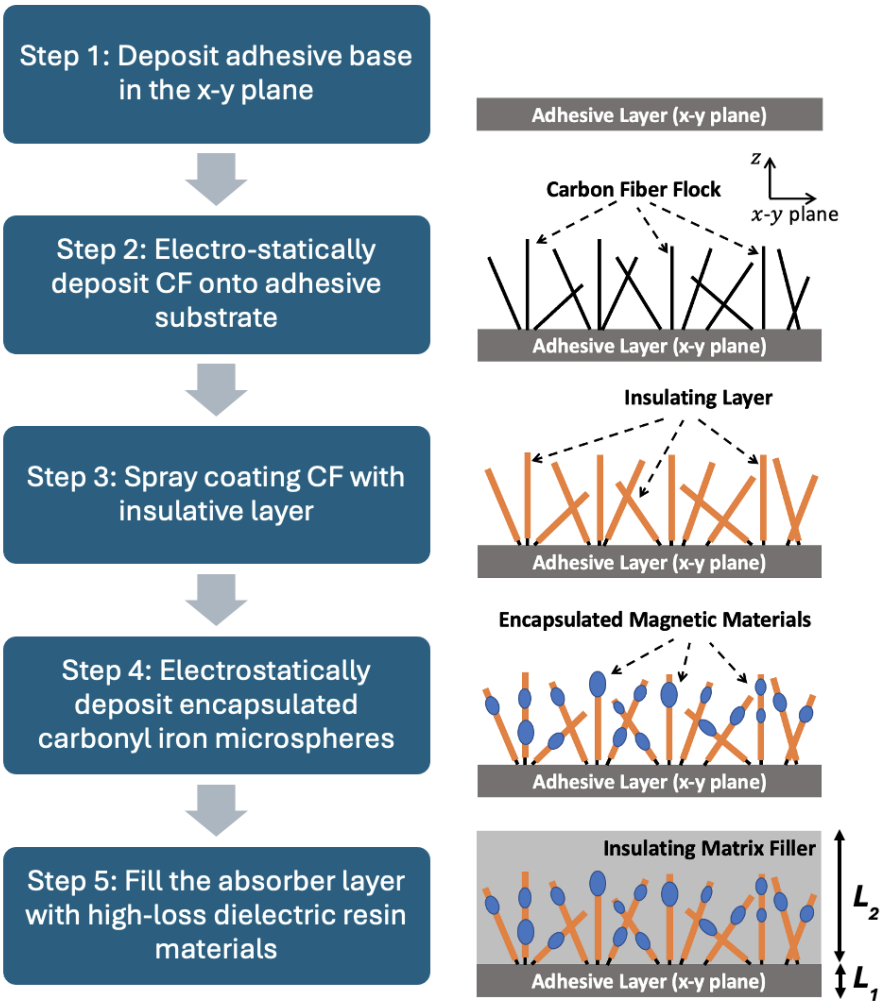

Fig. 1 Basic fabrication steps for developing magnetically loaded flocked CF absorber (MLF-CF) prototypes: Flow chart (left) and Illustration (right).

- **Step 4:** Electrostatically deposit carbonyl iron microspheres, combined with insulating materials, onto the vertical CF. This provides protection against wear, corrosion, and weather.
- **Step 5:** Fill the absorber layer with high-loss dielectric resin materials, such as epoxy, silicone, foams, aerogels, acrylic blends, or elastomers, depending on the product and application requirements. This step enhances the strength and durability of the absorber and is optional.

The deposition of a small amount of carbon fibers in this unique manner enables the reduction of overall conductivity in the absorber by maintaining low carbon fiber

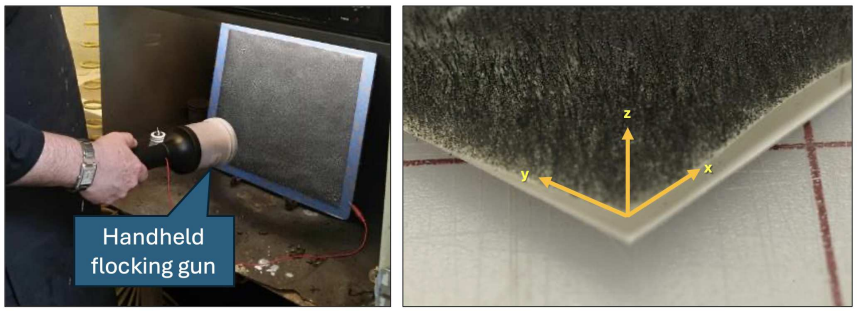

Fig. 2 Flocking process to electrostatically deposit CF onto the adhesive substrate (left) and the profile view of vertically flocked CF (right). The sample is placed on a white tray for photography.

density. High-conductivity materials attenuate signals traveling through them quickly, but they are unsuitable for absorbers as they reflect signals at the air-absorber interface. Another advantage of the flocking method is that it ensures carbon fiber is deposited along the z-axis. Experimental results demonstrate that this arrangement leads to better microwave absorption compared to carbon fiber deposited on the x-y plane. However, because the carbon fibers are deposited on top of an adhesive layer forming two distinctive layers, all characterization measurements must be conducted for two separate layers. We use two waveguide sets for X-band and Ku-band to investigate the absorber from 8 to 18 GHz. This requires 2 different sets of MLF-CF absorber samples which were chosen to have only small differences in their thicknesses. Even though the differences are small, they must be accounted for. Table 2 outlines the measured thickness of each MLF-CF sample and its layers, and the frequency band in which each sample was characterized in this study.

Table 2 Layer and sample thickness for different frequency setups. See Fig. 1 for L_1 and L_2 thickness definition

	MLF-CF sample 1 X-band	MLF-CF sample 2 Ku-band
L_1 - Substrate (mm)	1.08	1.06
L_2 - Flocked materials (mm)	3.27	3.36
L_{total} (mm)	4.35	4.42

As discussed in [10], one of the advantages of our MLF-CF absorbers is that they are lightweight. This advantage comes from using a relatively small amount of both carbon fibers as well as magnetic spheres. Table 3 compares the weights of our MLF-CF absorbers and a commercially available absorber (MR21-003-01) from MAST Technologies. It clearly shows that the MLF-CF provides a broader -10dB BW and similar F_{best} with a lower weight per area value. The MAST absorber was chosen for comparison since it has magnetic material loading. All of the materials used in the production

of MLF-CF are readily available and at relatively low cost. The manufacturing processes are generally well-established in other industries and easily scalable if increased production is required.

Table 3 Weights and thicknesses of MAST MR21 [16] and MLF-CF materials without filler [10] and with filler (this paper).

Absorber	Weight/Area (lb/ft^2)	Thickness (mm)	-10dB BW (GHz)	F_{best} (GHz)
MR21-0003-01	0.89	1	6	10.5
MLF-CF (no filler)	0.10	2	2.5	11.1
MLF-CF (with filler)	0.73	4.35-4.42	10	10.2

3 Theoretical Reflection Loss Calculation

Reflection loss (RL) is a key and often quoted metric used to describe the effectiveness of absorbers. It makes the comparison of absorber performance among different approaches and materials relatively straightforward. It is usually defined as the ratio of reflected over incident wave power. In this section, reflection loss calculation is presented for both waveguide and free-space measurement techniques. Fig. 3 describes a two-layer microwave absorber terminated by a perfect electric conductor in the back. We use transmission line theory to calculate the RL at the air-absorber interface first for the waveguide measurement and then for the free-space case. This calculation is based on the thickness of the two layers L_1, L_2 in Table 2 and the complex relative electric permittivity (ε_r) and magnetic permeability (μ_r) of each layer of the material.

For the reflection loss in waveguide measurement, the m^{th} layer of the absorber has characteristic impedance Z_m and propagation constant γ_m as follows [17]:

$$Z_m = \frac{1}{\sqrt{1-(fc_m/f)^2}}\sqrt{\frac{\mu_m\mu_0}{\varepsilon_m\varepsilon_0}} = \frac{Z_0}{\sqrt{1-(fc_m/f)^2}}\sqrt{\frac{\mu_m}{\varepsilon_m}} \tag{1}$$

$$\gamma_m = j\omega\sqrt{\mu_m\mu_0\varepsilon_m\varepsilon_0}\sqrt{1-(fc_m/f)^2} = j\frac{2\pi f}{c}\sqrt{\mu_m\varepsilon_m}\sqrt{1-(fc_m/f)^2} \tag{2}$$

where ε_m, μ_m are m^{th} layer relative permittivity and permeability, Z_0 is vacuum characteristic impedance, and c is speed of light. The TE_{10} cut-off frequency fc_m is calculated based on ε_m, μ_m, and waveguide dimensions a from Table 4, as shown in Eq. 3.

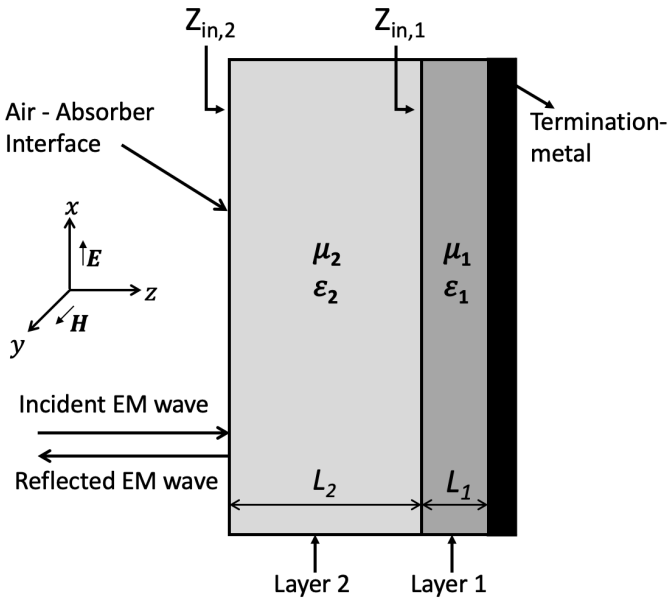

Fig. 3 Schematic of 2-layer absorber used for reflection loss analysis.

$$
\begin{aligned}
Z_0 &= \sqrt{\frac{\mu_0}{\varepsilon_0}} = 377\ \Omega\ ; \qquad c = \frac{1}{\sqrt{\mu_0 \varepsilon_0}} = 3 \times 10^8\ m/s \\
fc_1 &= \frac{1}{2a\sqrt{\mu_1 \mu_0 \varepsilon_1 \varepsilon_0}} = \frac{c}{2a\sqrt{\mu_1 \varepsilon_1}} \\
fc_2 &= \frac{1}{2a\sqrt{\mu_2 \mu_0 \varepsilon_2 \varepsilon_0}} = \frac{c}{2a\sqrt{\mu_2 \varepsilon_2}}
\end{aligned} \tag{3}
$$

By substituting Eq. 1, Eq. 2, and Eq. 3 into Eq. 4, we can calculate $Z_{in,m}$ for each layer with ε_m, μ_m are the m^{th} layer relative permittivity and permeability:

$$
Z_{in,m} = Z_m \frac{Z_{Load} + Z_m \tanh(\gamma_m L_m)}{Z_m + Z_{Load} \tanh(\gamma_m L_m)} \tag{4}
$$

At layer 1 with metal termination, $Z_{Load} = Z_{term} = 0\ \Omega$, the input impedance is obtained using Eq. 5 below:

$$
\begin{aligned}
Z_{in,1} &= Z_1 \tanh(\gamma_1 L_1) \\
&= \frac{Z_0}{\sqrt{1 - (fc_1/f)^2}} \sqrt{\frac{\mu_1}{\varepsilon_1}} \tanh\left(j L_1 \frac{2\pi f}{c} \sqrt{\mu_1 \varepsilon_1} \sqrt{1 - (fc_1/f)^2} \right)
\end{aligned} \tag{5}
$$

At layer 2, $Z_{in,1}$ then becomes Z_{Load} and input impedance $Z_{in,2}$ is calculated with Z_2 and γ_2 as:

$$
\begin{aligned}
Z_{in,2} &= Z_2 \frac{Z_{in,1} + Z_2 \tanh(\gamma_2 L_2)}{Z_2 + Z_{in,1} \tanh(\gamma_2 L_2)} \\
\text{where} \quad Z_2 &= \frac{Z_0}{\sqrt{1-(fc_2/f)^2}} \sqrt{\frac{\mu_2}{\varepsilon_2}} \\
\gamma_2 &= j\frac{2\pi f}{c} \sqrt{\mu_2 \varepsilon_2} \sqrt{1-(fc_2/f)^2}
\end{aligned}
\tag{6}
$$

The reflection loss of the absorber is calculated based on the mismatch between impedance $Z_{in,2}$ from the above equation and vacuum characteristic impedance in waveguide Z_{0WG}. The reflection loss obtained from Eq. 7 using extracted permittivity and permeability is then used for comparison with the reflection loss in the waveguide simulation from high-frequency structure simulator (HFSS) described in Section 5. *Note that in this paper we define reflection loss (RL) as a negative quantity in dB. Therefore, RL in Eq. 7 and Eq. 9 do not have the negative sign in front of them. This convention is followed throughout this paper for convenient comparison between analytical calculation, measurement, and simulation. Note that some authors prefer to use return loss which is the inverse of reflection loss (as defined here) which is a positive quantity in dB.*

$$
\begin{aligned}
\Gamma &= \frac{Z_{in,2} - Z_{0WG}}{Z_{in,2} + Z_{0WG}} ; \quad RL\ (dB) = 20 \log_{10} |\Gamma| \\
\text{where} \quad Z_{0WG} &= \frac{Z_0}{\sqrt{1-(fc_0/f)^2}} ; \quad fc_0 = \frac{c}{2a}
\end{aligned}
\tag{7}
$$

For the free-space case, we perform a similar analysis with Eq. 1 and Eq. 2 are replaced with Eq. 8. As a result, the reflection loss for the free space can be obtained using Eq. 9:

$$
\begin{aligned}
Z_{m-FS} &= \sqrt{\frac{\mu_m \mu_0}{\varepsilon_m \varepsilon_0}} = Z_0 \sqrt{\frac{\mu_m}{\varepsilon_m}} \\
\gamma_{m-FS} &= j\omega \sqrt{\mu_m \mu_0 \varepsilon_m \varepsilon_0} = j\frac{2\pi f}{c} \sqrt{\mu_m \varepsilon_m}
\end{aligned}
\tag{8}
$$

$$
\Gamma_{FS} = \frac{Z_{in,2-FS} - Z_0}{Z_{in,2-FS} + Z_0} ; \quad RL_{FS}\ (dB) = 20 \log_{10} |\Gamma_{FS}| \tag{9}
$$

4 Rectangular Waveguide Measurements and Absorber Parameters Extractions

4.1 Measurement Setup and Extraction Procedure

A Vector Network Analyzer (VNA) is utilized for measuring and analyzing Scattering parameters (S-parameters) of samples. The experimental setup involves placing a

sample holder between two straight waveguide sections. Fig. 4a shows the X-band and Ku-band waveguide sets employed in this paper. The cross-section dimensions (a, b) of each waveguide and frequency ranges are specified in Table 4. Before conducting the measurement, the VNA is calibrated to the sample holder using *Thru-Reflect-Line (TRL)* calibration. The *Thru* standard is achieved by connecting the two straight waveguide sections. We use a *Short* termination for each waveguide section with an aluminum plate for *Reflect* standard. It is crucial to ensure that the *Line* standard has the correct lambda quarter thickness ($L_{\lambda/4}$) for each waveguide band, as indicated in Table 4. Note that the quarter wavelength is calculated at the center frequency for each band. In practical situations, the thickness of the quarter-waveguide standard may deviate from the values specified in Table 4 due to factors such as manufacturer discrepancies or availability constraints. Despite the potential for these variations to be minor, it remains essential to precisely compute the accurate time delay for utilization in VNA standard calibration.

Table 4 Waveguide dimensions, frequency coverage, and quarter wavelength thickness used in calibration.

Band	X (WR-90)	Ku (WR-62)
Freq. (GHz)	8 - 12	12 - 18
a (mm)	22.86	15.80
b (mm)	10.16	7.90
$L_{\lambda/4}$ (mm)	9.7	6.44

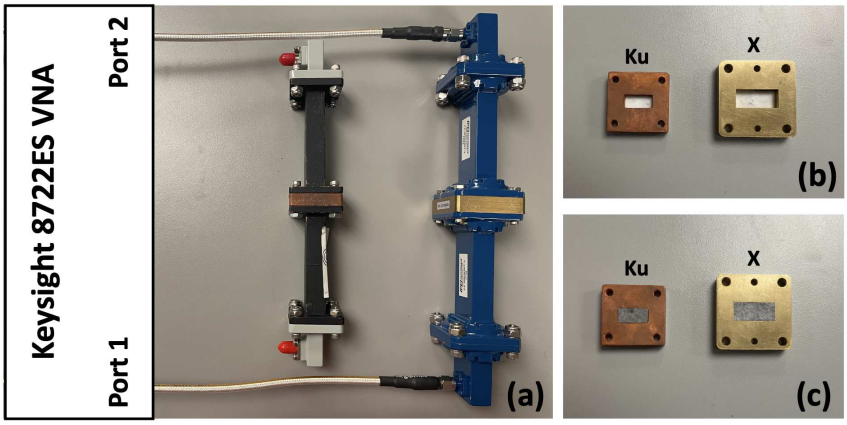

Fig. 4 (a) Waveguide measurement setup for X-band (waveguide set in blue) and Ku-band (waveguide set in black); (b) and (c) Materials under test (MUT) mounted in sample holders.

Additionally, the *Line* standard is employed as the sample holder in this experiment. Fig. 4b and c display the two sides of the sample holders with materials under test for both X and Ku bands. It is important to note that the thickness of the sample holder differs from the sample thickness (see Table 2 and 4). Therefore, a reference plane shift is necessary to account for the disparity between the sample and sample holder[18]. To simplify this process, we position the sample against one edge of the sample holder, which is connected to port 1 of the VNA. As a result, an open section of the sample holder, with a thickness of $L_{\lambda/4} - L_{total}$, is connected to port 2. Therefore, we apply a phase shift $\Delta\phi_{21}$ to the transmission coefficient S_{21} before extracting the parameters from the measurements. Using Eq. 10 together with sample thickness in Table 2 and quarter-wavelength sample holder thickness from Table 4, we obtain the phase shift for X-band as $\Delta\phi_{21-X} = 5.35\ mm \times 2\pi/\lambda$ and for Ku-band as $\Delta\phi_{21-Ku} = 2.02\ mm \times 2\pi/\lambda$.

$$\Delta\phi_{21} = (L_{\lambda/4} - L_{total}) \times \frac{2\pi}{\lambda} \tag{10}$$

We use the NRW algorithm to extract the complex relative permittivity and permeability of the samples.

$$\mu_r = \frac{1+\Gamma}{\Lambda(1-\Gamma)\sqrt{\frac{1}{\lambda_0^2} - \frac{1}{\lambda_c^2}}} \tag{11}$$

$$\varepsilon_r = \frac{\lambda_0^2}{\mu_r\left(\frac{1}{\lambda_c^2} - \frac{1}{\Lambda^2}\right)} \tag{12}$$

$$with \quad \frac{1}{\Lambda^2} = -\left[\frac{1}{2\pi L}\ln\left(\frac{1}{P}\right)\right]^2 \tag{13}$$

where λ_0 is the free-space wavelength, λ_c is the cutoff wavelength of the corresponding waveguide, and L is the thickness of the sample (i.e. L_1 or L_2 depending on which sample is measured).

Complex reflection coefficient Γ and the propagation factor P are calculated from measured S-parameters (Eq. 14, 15):

$$\Gamma = \chi \pm \sqrt{\chi^2 - 1} \ \ with \ \ \chi = \frac{S_{11}^2 - S_{21}^2 + 1}{2S_{11}} \tag{14}$$

$$P = \frac{S_{11} + S_{21} - \Gamma}{1 - (S_{11} + S_{21})\Gamma} \tag{15}$$

The collected S-parameters from the VNA exhibit phase ambiguity, specifically in the phase of S_{11} and S_{21}, which is confined to a range of $-\pi$ to $+\pi$. As a result, Eq. 13 can be satisfied by multiple solutions because the phase of the complex propagation factor P can be either increased or decreased by $2n\pi$. To identify the correct value for

n, it is crucial to search for the solution that aligns with the measured group delay specified in Eq. 16. This approach enables the determination of the accurate solution from the infinite possibilities available.

$$\begin{aligned} \tau_{g,n} &= L\frac{\mathrm{d}}{\mathrm{d}f}\left(\frac{\epsilon_r\mu_r}{\lambda_0^2} - \frac{1}{\lambda_c^2}\right)_n^{1/2} \\ \tau_g &= -\frac{1}{2\pi}.\frac{\mathrm{d}\phi}{\mathrm{d}f} \end{aligned} \tag{16}$$

We follow the above procedure for the waveguide-based extraction of MLF-CF absorber permeability μ_r and permittivity ε_r which is discussed in the next section.

4.2 Extraction Results from Waveguide Measurement for MLF-CF Absorber

Within this section, we present the extracted parameters derived from the waveguide measurements described above. Fig. 5 and Fig. 6 provide plots of the relative permittivity and permeability pertaining to layers L1 and L2 of the MLF-CF absorber samples, respectively. In both figures, the real and imaginary parts of relative permittivity are in red, while the blue lines represent the real and imaginary parts of relative permeability. As explained in section 2, layer L1 is the adhesive layer, while layer L2 contains CF, ferrite spheres, and filler.

For Layer L1, $\Re(\varepsilon_r)$ exhibits a value of approximately 3.2 in the X-band and maintains its values through Ku-band. The $\Im(\varepsilon_r)$ values are measured at 0.2 and also remain constant. This shows a small degree of dielectric loss in layer L1 in X-band and Ku-band frequency range. On the other hand, extracted values of μ_r show that the material in layer 1 of each sample is not magnetic, in other words, $\Re(\mu_r) = 1$ and $\Im(\mu_r) = 0$. Similarly, Fig. 6 represents the material properties of Layer L2 of the MLF-CF samples. Here, we observed a decreasing trend in $\Re(\varepsilon_r)$, ranging from 3.2 at 8.2 GHz to 2.8 at 18 GHz. The $\Im(\varepsilon_r)$ for Layer L2 is generally higher than that of Layer L1, remaining close to 0.5 across both frequency bands. The magnetic properties of Layer L2 also align with Layer L1, with $\Re(\mu_r)$ being approximately 1 and $\Im(\mu_r)$ close to 0.

Overall, the waveguide measurements indicate that the material losses are primarily attributed to the dielectric component. The magnetic contribution, represented by μ_r, remains around 1 for both Layer L1 and Layer L2, implying that magnetic properties do not significantly impact the reduction of reflection loss. However, it is crucial to note that experimentally we observe the need to include magnetic particles to obtain wideband characteristics. Therefore, the magnetic particles cannot be eliminated from the absorber construction. Through experiments, we notice that the increased use of magnetic loading tends to lower the frequency bands at which the broadband behavior of MLF-CF begins. This comes at a weight penalty due to the increased magnetic loading.

As indicated in Table 2, the sample thickness L_{total} is slightly different for different frequency ranges. From a practical perspective, waveguide measurements are sensitive to sample thickness and sample mounting. To improve the accuracy of the extraction,

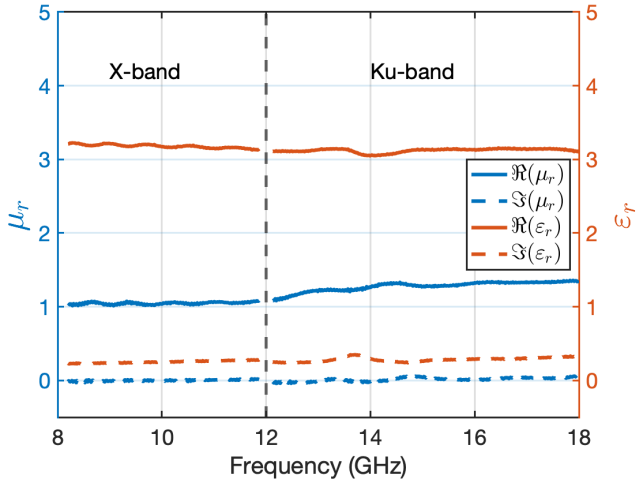

Fig. 5 Waveguide measurement of the relative permittivity (in red) and permeability (in blue) of the sample layer L1 at X and Ku bands.

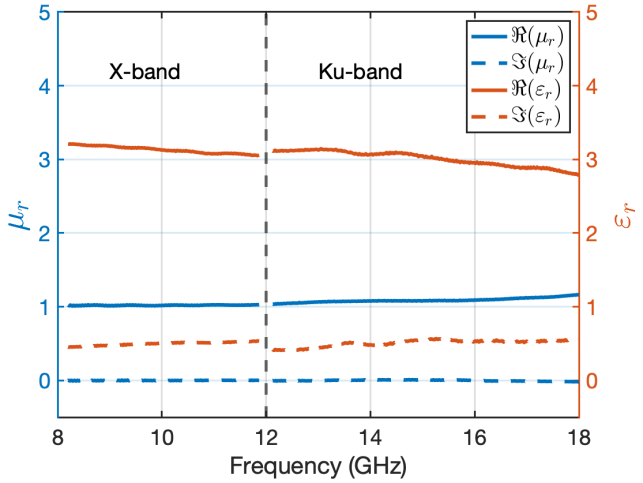

Fig. 6 Waveguide measurement of the relative permittivity (in red) and permeability (in blue) of the sample layer L2 at X and Ku bands.

it is essential to prepare and select samples that have minimum variation in thickness. Additionally, sample mounting plays an important role in the extraction process. Failing to properly mount the sample inside the waveguide will introduce air-gap which can lead to discontinuities at band transitions and inaccurate results.

5 Waveguide Simulation and Comparison with Measurements

5.1 Rectangular Waveguide Two-port Simulation using High-frequency Structure Simulator (HFSS)

Fig. 7 shows the simulation setup in HFSS [19]. This simulation aims to replicate the measurement done with VNA and rectangular waveguides. The goal of this simulation is to verify the extraction procedure. By comparing the simulated and measured S-parameters we can confirm that the extraction works well.

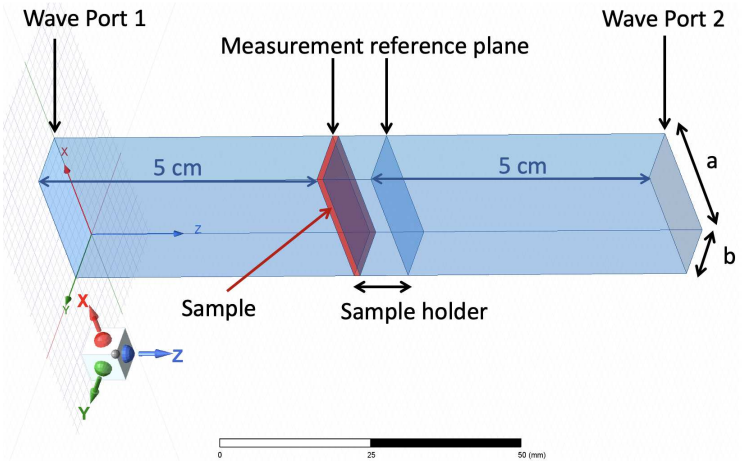

Fig. 7 HFSS setup for rectangular waveguide two-port simulation.

The simulation setup includes two wave ports at both ends to generate and receive signals. The cross-section of the port has waveguide dimensions a and b given in Table 4. Right after the two ports are 2 straight waveguide sections of 5 cm in length. In the middle is the sample holder and material under test. The thickness of the samples is given in Table 2.

In order to compare simulated and measured S-parameters, it is essential to match the reference plane of the two sets of S-parameters. In this case, we need to move the reference planes 5 cm toward the samples on both sides. The following $\Delta\phi_{11}$ and $\Delta\phi_{21}$ are applied to the simulated S_{11} and S_{21} coefficient respectively:

$$\Delta\phi_{11} = \Delta\phi_{21} \quad = (5\ cm + 5\ cm) \times \frac{2\pi}{\lambda} \tag{17}$$

where λ is the wavelength in the rectangular waveguide. Note that the amount of phase shift for S_{11} and S_{21} in this case are the same because the two straight waveguide sections are both 5 cm long.

Fig. 8 and Fig. 9 illustrate the simulated transmission parameter S_T and reflection parameter S_R in comparison with measured parameters for X-band (8-12 GHz) and

Ku-band (12-18 GHz) for layers L1 and L2 of the MLF-CF samples respectively. In both figures, the magnitude is represented in blue and the phase is in red. The measured results are plotted in dash lines and the simulated parameters are shown in dots.

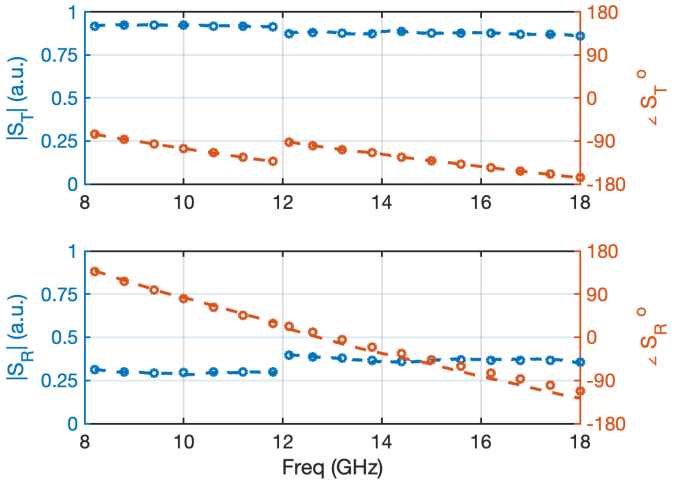

Fig. 8 Simulated phase and magnitude results (dotted) compared with measurement (dash) of sample layer L1 at X and Ku bands.

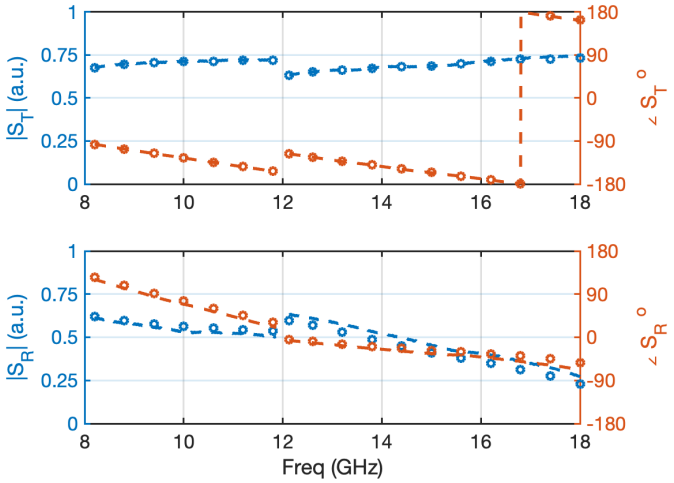

Fig. 9 Simulated phase and magnitude results (dotted) compared with measurement (dash) of sample layer L2 at X and Ku bands.

In Fig. 8, the comparison for sample layer L1 indicates an excellent agreement between the simulation and the measurement. The magnitude of S_T gradually decreases from 0.92 at 8 GHz to 0.86 at 18 GHz, with a small discontinuity at 12 GHz due to the change in waveguide setup from X-band to Ku-band. S_T phase has the same discontinuity at the transition but holds the declining slope across two frequency bands. For reflection parameter S_R, even though its magnitude at Ku-band is slightly higher than X-band, we can still observe the slowly decreasing trend among both frequency bands. On the other hand, the S_R phase displays a perfect agreement between simulation and measurement with negligible discontinuity at the transition frequency.

The simulation results plotted in Fig. 9 also satisfactorily agree with the measured parameters for sample layer L2. S_T magnitude increases from 0.67 to 0.73 across both frequency bands while S_R decreases from 0.62 at 8 GHz to 0.23 at 18 GHz. Similar to sample layer L1, both magnitude and phase have a small mismatch at 12 GHz, but their increasing and decreasing tendencies remain across X-band and Ku-Band. Hence, the waveguide measurements of transmission and reflection parameters (both magnitude and phase) agree well with the waveguide simulation of the same parameters for both L1 and L2 layers of the MLF-CF samples.

5.2 Waveguide Reflection Loss Simulation using HFSS

Another HFSS simulation was also performed to verify the reflection loss calculation described in Sec 3. Fig. 10 illustrates the setup for 3D reflection loss simulation in HFSS. Here, a wave port is placed at the input of the waveguide, followed by a 5 cm waveguide section and then the two layers of the sample. The other end of the waveguide is shorted using perfect electric conductor (PEC) boundary conditions. Similar to the two port simulation, the reflection loss S_{11} requires $\Delta\phi_{11}$ phase shift in Eq. 17.

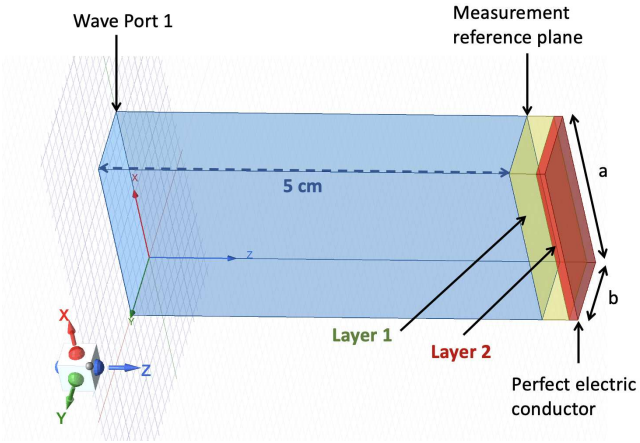

Fig. 10 HFSS setup for shorted rectangular waveguide simulation.

Fig. 11 compares reflection loss parameters S_R obtained from the 3D simulation described above and analytical calculation from Sec. 3. For both cases, the two layers

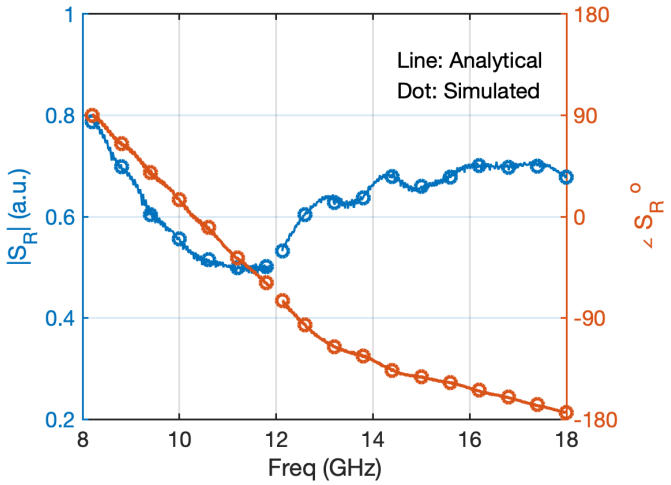

Fig. 11 Rectangular waveguide reflection loss comparison between HFSS simulation and analytical equation calculation of the whole MLF-CF prototype for X and Ku bands.

(L1 and L2) are combined into one whole MLF-CF prototype with the material parameters for each layer ε and μ extracted from rectangular waveguide measurements. We can observe that the analytical and simulated reflection losses are the same. Thus, it is demonstrated that the reflection loss calculation using transmission line theory is applicable in the rectangular waveguide environment.

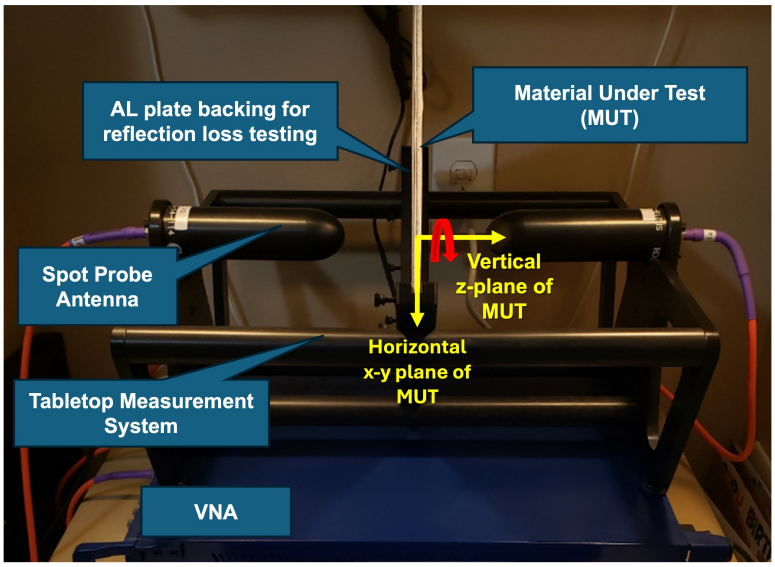

Fig. 12 Spot probe system setup for free-space reflection loss measurement. Photo: TangiTek, LLC.

6 Free-space Reflection Loss Measurement and Analysis

In this section, the measurement and calculation of the reflection loss (RL) for the MLF-CF absorber in free space is presented. Fig. 12 demonstrates the setup using a spot probe system to measure the reflection loss across the frequency range of 8 to 18 GHz [20]. The spot probe is placed at normal incidence to the material under test (MUT) surface. Free-space RL measurements are performed with a metal backing to explore the efficiency of the MLF-CF absorber in terms of preventing signal reflection from the metal. The MLF-CF absorber is anisotropic. To characterize material anisotropy, we perform the free-space RL measurements with different MUT rotations. As illustrated in Fig. 12, the MLF-CF absorber is rotated around its vertical z-axis in 90^0 increments while keeping the absorber perpendicular to the direction of wave propagation. Reflection loss measurements are made after each MUT rotation about its vertical z-axis.

Fig. 13 displays the reflection loss of MLF-CF absorber under different rotations. The MLF-CF absorber achieves a reflection loss of less than -10dB over a wide frequency band from 8 to 18 GHz. Additionally, there are two resonance points at around 10 and 18 GHz, with corresponding RL values of -36 dB and -32 dB, respectively. The rotational variability effects are clearly present in Fig. 13 with several rotating angles of the MLF-CF prototype. In X-band, the RL at the resonance point changes from -27 dB at 180^o rotation to -36 dB at 270^o rotation. For Ku-band, the difference in RL at resonance is smaller than in X-band, but the variation in resonant frequency is larger. Compared to our previously reported results [10, 11] these results are much more consistent. However, the RL is less than -10 dB across X and Ku bands, and less than -17 dB across an octave from 9 GHz to 18 GHz, independent of orientation. These free-space spot probe measurements of reflection loss demonstrate that MLF-CF has broadband performance of -10 dB RL over the entire X and Ku bands.

The analytically calculated reflection loss of MLF-CF in X-band is displayed in Fig. 14. The plot is generated with the material properties (ε_r, μ_r) of each layer extracted from the waveguide measurements described in Section 4.2. To account for thickness variability, we vary the thickness of layer L2 and calculate the corresponding reflection loss. We observe the expected low reflection loss region (resonance point) in X-band, with the depth of the lowest point being influenced by the thickness. For instance, from Fig. 14, the analytical calculations show that a MLF-CL sample with L2 thickness of 2.9±0.4 mm will provide a RL of -10 dB or more in the 10 to 12 GHz frequency range in X-band. This is consistent with overall gross spot-probe reflection loss measurements presented in Fig. 13. However, some discrepancies in the reflection loss values from spot probe measurements and analytical calculations are still noticeable. The main reason for this difference is the anisotropic effect as observed in spot probe measurement as shown in Fig. 13. Since the resonance frequency and reflection loss values change with rotation, it's difficult to find a unique set of parameters to fully describe the material. Moreover, the location from which waveguide samples are cut and used to extract material parameters may also affect results due to material variations across

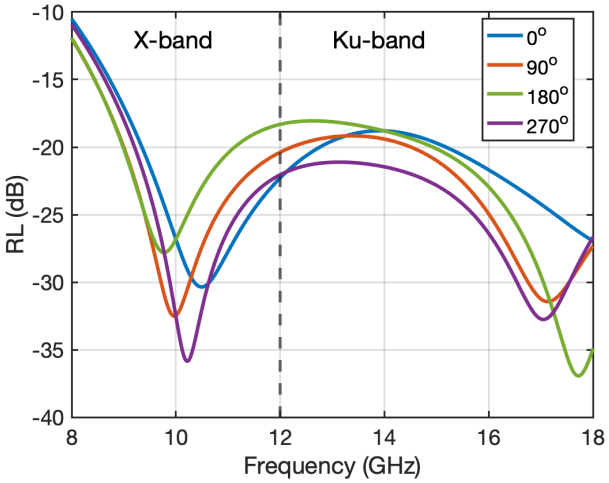

Fig. 13 RL of MLF-CF prototype from spot probe system with 4 different sample rotations.

the whole sample. These challenges will be addressed in future work through improved manufacturing, inclusion of anisotropic effects, and more detailed sensitivity analysis.

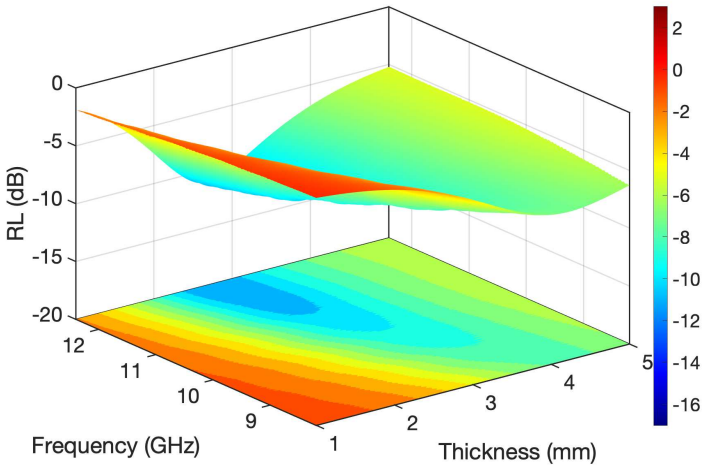

Fig. 14 Calculated free space RL in X-band of MLF-CF prototype based on rectangular waveguide measurement and extracted permittivity and permeability with variable layer two (L2) thickness.

Overall, these results illustrate that the extracted parameters can be used to predict absorber performance and optimize the absorber thickness. However, slight differences arise due to the variation in the nature of propagating waves. While the E- and H-fields are perpendicular to the carbon fibers in free space propagation, this is no longer true in a waveguide setup. Therefore, it is advisable to employ the same excitation wave for

accurate comparisons. Furthermore, Fig. 14 demonstrates the scalability of the MLF-CF absorber, where thinner thicknesses result in higher resonance frequencies. While this calculation has many built-in approximations, it is nonetheless useful in guiding future development and optimization of the MLF-CF absorbers.

7 Conclusion

By using advanced materials and designs, it is possible to minimize EMI and reduce electromagnetic pollution, thereby enabling the safe and reliable operation of wireless technologies. This paper presents the development and characterization of an innovative ultra-wideband microwave absorber material utilizing ferrite beads and carbon fibers. The combination of these materials and the manufacturing process results in a low-cost, lightweight, and broadband absorber design. The prototype is prepared using a flocking process, where its components are electrostatically deposited onto a substrate, therefore called magnetically loaded flock carbon fiber (MLF-CF) absorber.

The characterization of the MLF-CF absorber involves the analysis of distinct material properties in two separate layers. Rectangular waveguide measurements are conducted at X-band and Ku-band, employing transverse electric waves (TE_{10}) to obtain the complex electric permittivity and magnetic permeability of the samples. Additional analysis is performed by comparing measured and HFSS simulated S-parameters to verify the extraction procedure.

The extracted material properties from rectangular waveguide characterization techniques are then incorporated into analytical equations to estimate the reflection loss (RL). The calculated RL is subsequently compared with experimental measurements conducted using a spot probe system. The results obtained from the spot probe system validate the performance of the absorber, demonstrating its ability to maintain a minimum RL of -10 dB across the X and Ku frequency bands. However, discrepancies between the analytical RL and spot-probe measured RL indicate that details of our model need to be refined.

In conclusion, this study highlights the potential of carbon fibers and ferrite beads as a promising combination for the development of low-cost and lightweight microwave absorber materials suitable for wideband frequency applications. In the future, we plan to explore different combinations and ratios of carbon fibers, ferrite beads, and filler materials to achieve an optimal design for a microwave absorber that is lightweight and even thinner but maintains a broadband -10dB reflection loss.

Acknowledgements. This work was supported in part by the National Science Foundation Grant No. 1721863 and OBDD/Business Oregon Grant No. C2018103.

We are thankful to Glenn LeBrasseur and Edward Ivory for their help in accessing the anechoic chamber at Portland State University (PSU). We would also like to express our appreciation to Phillip Wong for his support in lab instrumentations at PSU.

Declarations

- Funding: This work was supported in part by the National Science Foundation Grant No. 1721863 and OBDD/Business Oregon Grant No. C2018103.
- Conflict of interest/Competing interests: The authors declare no competing interests
- Ethics approval and consent to participate: Not applicable
- Consent for publication: Not applicable
- Data availability: Upon request
- Materials availability: Upon request
- Code availability: Upon request
- Author contribution: H.T.: Experiment planning, conducting measurements, performing analysis and simulation/modeling, writing, reviewing and editing manuscripts; B.P.: Funding acquisition, project administration and supervising, reviewing and editing manuscripts; R.D., K.T., A.R.: Funding, material fabrication, measurements, reviewing and editing manuscripts.

References

[1] He, Y., Gong, R., Cao, H., Wang, X., Zheng, Y.: Preparation and microwave absorption properties of metal magnetic micropowder-coated honeycomb sandwich structures **16**(5), 1501

[2] Yadav, R., Panwar, R.: Effective Medium Approximation Fused Optimization Strategy Derived New Kind of Honeycomb Microwave Absorbing Structure. IEEE Transactions on Magnetics **58**(3), 1–11 (2022) https://doi.org/10.1109/TMAG.2022.3140932

[3] Luo, H., Chen, F., Wang, F., Wang, X., Dai, W., Hu, S., Gong, R.: Preparation and microwave absorption properties of honeycomb core structures coated with composite absorber. AIP Advances **8**(5) (2018)

[4] Gorai, A., Mandal, R., Mandal, D.: Enhanced Electromagnetic Wave Absorption by Bi-Layered Nano-Hollow Spheres. IEEE Transactions on Magnetics **58**(8), 1–6 (2022) https://doi.org/10.1109/TMAG.2022.3144601

[5] Yadav, R., Panwar, R.: Multilayer Gradient Perforated Radar Absorbing Structure for Stealth Applications. IEEE Transactions on Magnetics **58**(2), 1–5 (2022) https://doi.org/10.1109/TMAG.2021.3103133

[6] D'Aloia, A.G., D'Amore, M., Sarto, M.S.: Oblique Incidence Optimal Design of Microwave Dielectric-Magnetic Absorbing Composites. IEEE Transactions on Magnetics **58**(5), 1–7 (2022) https://doi.org/10.1109/TMAG.2022.3157599

[7] Singh, J., Singh, C., Kaur, D., Narang, S.B., Jotania, R.B., Kagdi, A., Joshi, R., Bezerra Sombra, A.S., Zhou, D., Trukhanov, S., Panina, L., Trukhanov, A.: Optimization of Performance Parameters of Doped Ferrite-Based Microwave

Absorbers: Their Structural, Tunable Reflection Loss, Bandwidth, and Input Impedance Characteristics. IEEE Transactions on Magnetics **57**(7), 1–19 (2021) https://doi.org/10.1109/TMAG.2021.3063175

[8] Bhongale, S.R., Ingavale, H.R., Shinde, T.J., Pubby, K., Bindra Narang, S., Vasambekar, P.N.: X-Band Microwave Absorption in Nd^{3+}-Substituted Mg–Cd Spinel Ferrites Synthesized Under Microwave Sintering. IEEE Transactions on Magnetics **56**(10), 1–7 (2020) https://doi.org/10.1109/TMAG.2020.3014057

[9] Chen, X., Gu, Y., Liang, J., Bai, M., Wang, S., Li, M., Zhang, Z.: Enhanced microwave shielding effectiveness and suppressed reflection of chopped carbon fiber felt by electrostatic flocking of carbon fiber. Composites Part A: Applied Science and Manufacturing **139**, 106099 (2020) https://doi.org/10.1016/j.compositesa.2020.106099

[10] Tran, H., Le, T., Pejcinovic, B., Brown, J., Doneker, R., Thompson, K.G.R.: Characterization of Novel Magnetically Loaded Flocked Carbon Fiber Microwave Absorber. In: 2018 IEEE Symposium on Electromagnetic Compatibility, Signal Integrity and Power Integrity (EMC, SI PI), Long Beach, CA, pp. 41–46 (2018). https://doi.org/10.1109/EMCSI.2018.8495186

[11] Le, T., Tran, H., Pejcinovic, B., Thompson, K.G.R., Doneker, R., Ramachandran, A.: Development and characterization of carbon-fiber based magnetically loaded microwave absorber material. In: 2018 International Symposium on Electromagnetic Compatibility (EMC EUROPE), pp. 767–771 (2018). https://doi.org/10.1109/EMCEurope.2018.8485065

[12] Nicolson, A.M., Ross, G.F.: Measurement of the Intrinsic Properties of Materials by Time-Domain Techniques. IEEE Transactions on Instrumentation and Measurement **19**(4), 377–382 (1970) https://doi.org/10.1109/TIM.1970.4313932

[13] Weir, W.B.: Automatic measurement of complex dielectric constant and permeability at microwave frequencies. Proceedings of the IEEE **62**(1), 33–36 (1974) https://doi.org/10.1109/PROC.1974.9382

[14] Baker-Jarvis, J., Vanzura, E.J., Kissick, W.A.: Improved technique for determining complex permittivity with the transmission/reflection method. IEEE Transactions on Microwave Theory and Techniques **38**(8), 1096–1103 (1990) https://doi.org/10.1109/22.57336

[15] Chalapat, K., Sarvala, K., Li, J., Paraoanu, G.S.: Wideband Reference-Plane Invariant Method for Measuring Electromagnetic Parameters of Materials. IEEE Transactions on Microwave Theory and Techniques **57**(9), 2257–2267 (2009) https://doi.org/10.1109/TMTT.2009.2027160

[16] Mast Technologies. https://www.masttechnologies.com/products/defense/rf-absorbers/cavity-resonance-0-040-2/ Accessed 2024-04-30

[17] Pozar, D.M.: Microwave Engineering; 3rd Ed. Wiley, Hoboken, NJ (2005)

[18] HP: Materials Measurement: Measuring the Dielectric Constant of Solids with HP 8510 Network Analyzer (1985)

[19] HFSS. https://www.ansys.com/products/electronics/ansys-hfss Accessed 2024-05-15

[20] Schultz, J.W., Maloney, J.G., Maloney, K., Schultz, R.: A comparison of material measurement accuracy of RF spot probes to a lens-based focused beam system. In: Proc. 2014 AMTA Symposium (2014)